

1 MedMNIST v2 - A large-scale lightweight benchmark 2 for 2D and 3D biomedical image classification

3 Jiancheng Yang¹, Rui Shi¹, Donglai Wei², Zequan Liu³, Lin Zhao⁴, Bilian Ke⁵, Hanspeter
4 Pfister⁶, and Bingbing Ni¹

5 ¹Shanghai Jiao Tong University, Shanghai, China

6 ²Boston College, Chestnut Hill, MA

7 ³RWTH Aachen University, Aachen, Germany

8 ⁴Department of Endocrinology and Metabolism, Fudan Institute of Metabolic Diseases, Zhongshan Hospital, Fudan
9 University, Shanghai, China

10 ⁵Department of Ophthalmology, Shanghai General Hospital, Shanghai Jiao Tong University School of Medicine,
11 Shanghai, China

12 ⁶Harvard University, Cambridge, MA

13 *corresponding author(s): Bingbing Ni (nibingbing@sjtu.edu.cn)

14 ABSTRACT

We introduce *MedMNIST v2*, a large-scale MNIST-like dataset collection of standardized biomedical images, including 12 datasets for 2D and 6 datasets for 3D. All images are pre-processed into a small size of 28×28 (2D) or $28 \times 28 \times 28$ (3D) with the corresponding classification labels so that no background knowledge is required for users. Covering primary data modalities in biomedical images, MedMNIST v2 is designed to perform classification on lightweight 2D and 3D images with various dataset scales (from 100 to 100,000) and diverse tasks (binary/multi-class, ordinal regression, and multi-label). The resulting dataset, consisting of 708,069 2D images and 9,998 3D images in total, could support numerous research / educational purposes in biomedical image analysis, computer vision, and machine learning. We benchmark several baseline methods on MedMNIST v2, including 2D / 3D neural networks and open-source / commercial AutoML tools. The data and code are publicly available at <https://medmnist.com/>.

16 Background & Summary

17 Deep learning based biomedical image analysis plays an important role in the intersection of artificial intelligence and
18 healthcare¹⁻³. Is deep learning a panacea in this area? Because of the inherent complexity in biomedicine, data modalities,
19 dataset scales and tasks in biomedical image analysis could be highly diverse. Numerous biomedical imaging modalities are
20 designed for specific purposes by adjusting sensors and imaging protocols. The biomedical image dataset scales in biomedical
21 image analysis could range from 100 to 100,000. Moreover, even only considering medical image classification, there are
22 binary/multi-class classification, multi-label classification, and ordinal regression. As a result, it needs large amounts of
23 engineering effort to tune the deep learning models in real practice. On the other hand, it is not easy to identify whether a
24 specific model design could be generalizable if it is only evaluated on a few datasets. Large and diverse datasets are urged by
25 the research communities to fairly evaluate generalization performance of models.

26 Benchmarking data-driven approaches on various domains has been addressed by researchers. Visual Domain Decathlon
27 (VDD)⁴ develops an evaluation protocol on 10 existing natural image datasets to assess the model generalizability on different
28 domains. In medical imaging area, Medical Segmentation Decathlon (MSD)⁵ introduces 10 3D medical image segmentation
29 datasets to evaluate end-to-end segmentation performance: from whole 3D volumes to targets. It is particularly important
30 to understand the end-to-end performance of the current state of the art with MSD. However, the contribution of each part
31 in the end-to-end systems could be particularly hard to analyze. As reported in the winning solutions^{6,7}, hyperparameter
32 tuning, pre/post-processing, model ensemble strategies and training/test-time augmentation could be more important than
33 the machine learning part (*e.g.*, model architectures, learning scheme). Therefore, a large but simple dataset focusing on the
34 machine learning part like VDD, rather than the end-to-end system like MSD, will serve as a better benchmark to evaluate the
35 generalization performance of the machine learning algorithms on the medical image analysis tasks.

36 In this study, we aim at a new “decathlon” dataset for biomedical image analysis, named *MedMNIST v2*. As illustrated in
37 Figure 1, MedMNIST v2 is a large-scale benchmark for 2D and 3D biomedical image classification, covering 12 2D datasets
38 with 708,069 images and 6 3D datasets with 9,998 images. It is designed to be:

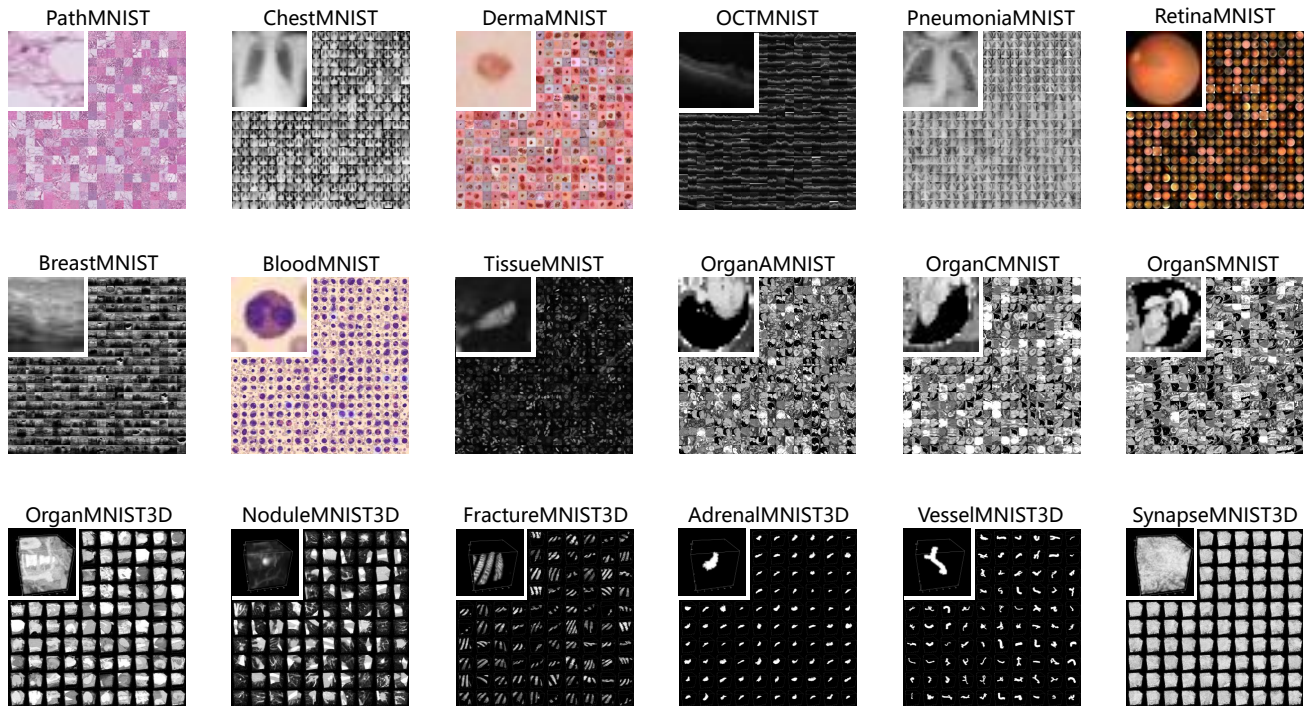


Figure 1. An overview of MedMNIST v2. MedMNIST is a large-scale MNIST-like collection of standardized 2D and 3D biomedical images with classification labels. It is designed to be diverse, standardized, educational, and lightweight, which could support numerous research / educational purposes.

- 39 • **Diverse:** It covers diverse data modalities, dataset scales (from 100 to 100,000), and tasks (binary/multi-class, multi-label,
40 and ordinal regression). It is as diverse as the VDD⁴ and MSD⁵ to fairly evaluate the generalizable performance of
41 machine learning algorithms in different settings, but both 2D and 3D biomedical images are provided.
- 42 • **Standardized:** Each sub-dataset is pre-processed into the same format (see details in Methods), which requires no
43 background knowledge for users. As an MNIST-like⁸ dataset collection to perform classification tasks on small images,
44 it primarily focuses on the machine learning part rather than the end-to-end system. Furthermore, we provide standard
45 train-validation-test splits for all datasets in MedMNIST v2, therefore algorithms could be easily compared.
- 46 • **Lightweight:** The small size of 28×28 (2D) or $28 \times 28 \times 28$ (3D) is friendly to evaluate machine learning algorithms.
- 47 • **Educational:** As an interdisciplinary research area, biomedical image analysis is difficult to hand on for researchers
48 from other communities, as it requires background knowledge from computer vision, machine learning, biomedical
49 imaging, and clinical science. Our data with the Creative Commons (CC) License is easy to use for educational purposes.

50 MedMNIST v2 is extended from our preliminary version, MedMNIST v1⁹, with 10 2D datasets for medical image
51 classification. As MedMNIST v1 is more medical-oriented, we additionally provide 2 2D bioimage datasets. Considering the
52 popularity of 3D imaging in biomedical area, we carefully develop 6 3D datasets following the same design principle as 2D ones.
53 A comparison of the “decathlon” datasets could be found in Table 1. We benchmark several standard deep learning methods
54 and AutoML tools with MedMNIST v2 on both 2D and 3D datasets, including ResNets¹⁰ with early-stopping strategies on
55 validation set, open-source AutoML tools (auto-sklearn¹¹ and AutoKeras¹²) and a commercial AutoML tool, Google AutoML
56 Vision (for 2D only). All benchmark experiments are repeated at least 3 times for more stable results than in MedMNIST v1.
57 Besides, the code for MedMNIST has been refactored to make it more friendly to use.

58 As a large-scale benchmark in biomedical image analysis, MedMNIST has been particularly useful for machine learning and
59 computer vision research^{13–15}, *e.g.*, AutoML, trustworthy machine learning, domain adaptive learning. Moreover, considering
60 the scarcity of 3D image classification datasets, the MedMNIST3D in MedMNIST v2 from diverse backgrounds could benefit
61 research in 3D computer vision.

Table 1. A comparison of MedMNIST v2 and other “decathlon” datasets.

	Visual Domain Decathlon ⁴	Medical Segmentation Decathlon ⁵	MedMNIST v1 ⁹	MedMNIST v2
Domain	Natural	Medical	Medical	Medical
Task	Classification	Segmentation	Classification	Classification
Datasets	10	10	10	18
2D / 3D	2D	3D	2D	2D & 3D
Image Size	Variable ($\approx 72^2$)	Variable ($\approx (30 - 300)^3$)	Fixed (28^2)	Fixed (28^2 & 28^3)

62 Methods

63 Design Principles

64 The MedMNIST v2 dataset consists of 12 2D and 6 3D standardized datasets from carefully selected sources covering primary
65 data modalities (*e.g.*, X-ray, OCT, ultrasound, CT, electron microscope), diverse classification tasks (binary/multi-class, ordinal
66 regression, and multi-label) and dataset scales (from 100 to 100,000). We illustrate the landscape of MedMNIST v2 in Figure 2.
67 As it is hard to categorize the data modalities, we use the imaging resolution instead to represent the modality. The diverse
68 dataset design could lead to diverse task difficulty, which is desirable as a biomedical image classification benchmark.

69 Although it is fair to compare performance on the test set only, it could be expensive to compare the impact of the
70 train-validation split. Therefore, we provide an official train-validation-test split for each subset. We use the official data split
71 from source dataset (if provided) to avoid data leakage. If the source dataset has only a split of training and validation set, we
72 use the official validation set as test set and split the official training set with a ratio of 9:1 into training-validation. For the
73 dataset without an official split, we split the dataset randomly at the patient level with a ratio of 7:1:2 into training-validation-test.
74 All images are pre-processed into a MNIST-like format, *i.e.*, 28×28 (2D) or $28 \times 28 \times 28$ (3D), with cubic spline interpolation
75 operation for image resizing. The MedMNIST uses the classification labels from the source datasets directly in most cases, but
76 the labels could be simplified (merged or deleted classes) if the classification tasks on the small images are too difficult. All
77 source datasets are either associated with the Creative Commons (CC) Licenses or developed by us, which allows us to develop
78 derivative datasets based on them. Some datasets are under CC-BY-NC license; we have contacted the authors and obtained the
79 permission to re-distribute the datasets.

80 We list the details of all datasets in Table 2. For simplicity, we call the collection of all 2D datasets as MedMNIST2D, and
81 that of 3D as MedMNIST3D. In the next sections, we will describe how each dataset is created.

Table 2. Data summary of MedMNIST v2 dataset, including data source, data modality, type of the classification task together with the number of classes for multi-class or that of labels for multi-label, number of samples in total and in each data split (training/validation/test). Upper: MedMNIST2D, 12 datasets of 2D images. Lower: MedMNIST3D, 6 datasets of 3D images. MC: Multi-Class. BC: Binary-Class. ML: Multi-Label. OR: Ordinal Regression.

Name	Source	Data Modality	Task (# Classes / Labels)	# Samples	# Training / Validation / Test
<i>MedMNIST2D</i>					
PathMNIST	Kather et al. ^{16,17}	Colon Pathology	MC (9)	107,180	89,996 / 10,004 / 7,180
ChestMNIST	Wang et al. ¹⁸	Chest X-Ray	ML (14) BC (2)	112,120	78,468 / 11,219 / 22,433
DermaMNIST	Tschandl et al. ^{19,20} , Codella et al. ²¹	Dermatoscope	MC (7)	10,015	7,007 / 1,003 / 2,005
OCTMNIST	Kermany et al. ^{22,23}	Retinal OCT	MC (4)	109,309	97,477 / 10,832 / 1,000
PneumoniaMNIST	Kermany et al. ^{22,23}	Chest X-Ray	BC (2)	5,856	4,708 / 524 / 624
RetinaMNIST	DeepDRiD Team ²⁴	Fundus Camera	OR (5)	1,600	1,080 / 120 / 400
BreastMNIST	Al-Dhabyani et al. ²⁵	Breast Ultrasound	BC (2)	780	546 / 78 / 156
BloodMNIST	Acevedo et al. ^{26,27}	Blood Cell Microscope	MC (8)	17,092	11,959 / 1,712 / 3,421
TissueMNIST	Ljosa et al. ²⁸	Kidney Cortex Microscope	MC (8)	236,386	165,466 / 23,640 / 47,280
OrganAMNIST	Bilic et al. ²⁹ , Xu et al. ³⁰	Abdominal CT	MC (11)	58,850	34,581 / 6,491 / 17,778
OrganCMNIST	Bilic et al. ²⁹ , Xu et al. ³⁰	Abdominal CT	MC (11)	23,660	13,000 / 2,392 / 8,268
OrganSMNIST	Bilic et al. ²⁹ , Xu et al. ³⁰	Abdominal CT	MC (11)	25,221	13,940 / 2,452 / 8,829
<i>MedMNIST3D</i>					
OrganMNIST3D	Bilic et al. ²⁹ , Xu et al. ³⁰	Abdominal CT	MC (11)	1,743	972 / 161 / 610
NoduleMNIST3D	Armato et al. ³¹	Chest CT	BC (2)	1,633	1,158 / 165 / 310
AdrenalMNIST3D	New	Shape from Abdominal CT	BC (2)	1,584	1,188 / 98 / 298
FractureMNIST3D	Jin et al. ³²	Chest CT	MC (3)	1,370	1,027 / 103 / 240
VesselMNIST3D	Yang et al. ³³	Shape from Brain MRA	BC (2)	1,909	1,335 / 192 / 382
SynapseMNIST3D	New	Electron Microscope	BC (2)	1,759	1,230 / 177 / 352

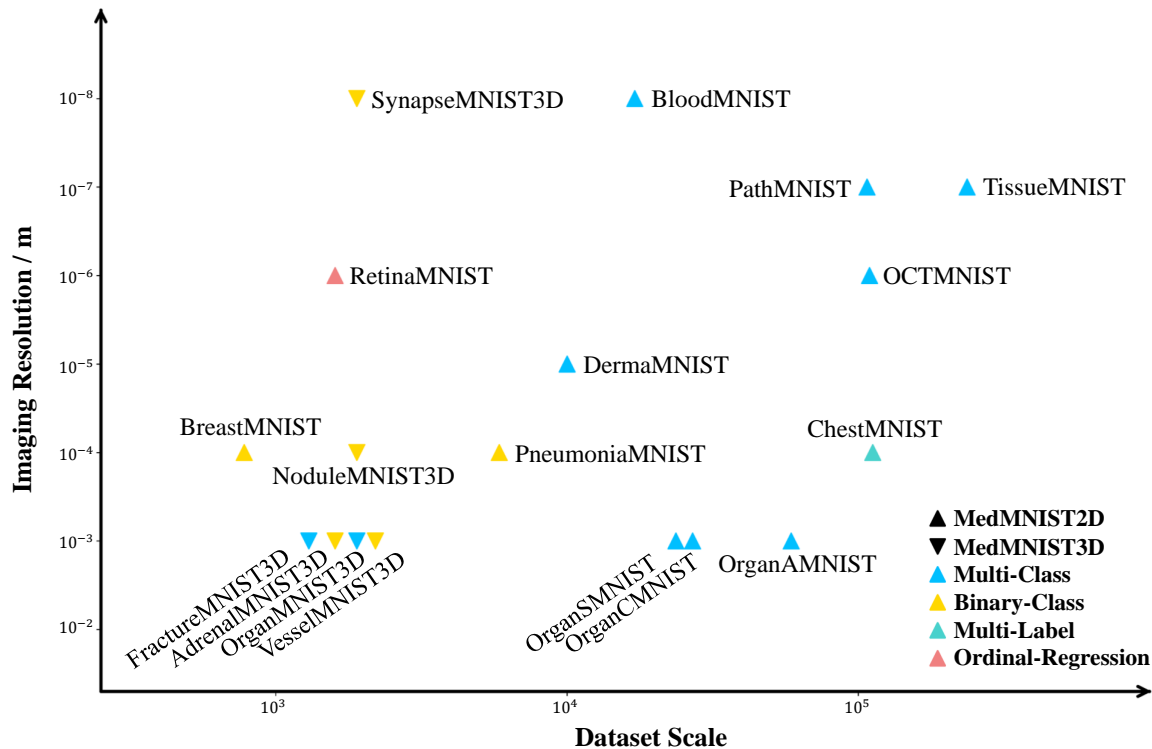


Figure 2. The landscape of MedMNIST v2. The horizontal axis denotes the base-10 logarithm of the dataset scale, and the vertical axis denotes base-10 logarithm of imaging resolution. The upward and downward triangles are used to distinguish between 2D datasets and 3D datasets, and the 4 different colors represent different tasks.

82 Details for MedMNIST2D

83 *PathMNIST*

84 The PathMNIST is based on a prior study^{16,17} for predicting survival from colorectal cancer histology slides, providing a dataset
 85 (NCT-CRC-HE-100K) of 100,000 non-overlapping image patches from hematoxylin & eosin stained histological images, and
 86 a test dataset (CRC-VAL-HE-7K) of 7,180 image patches from a different clinical center. The dataset is comprised of 9 types
 87 of tissues, resulting in a multi-class classification task. We resize the source images of $3 \times 224 \times 224$ into $3 \times 28 \times 28$, and split
 88 NCT-CRC-HE-100K into training and validation set with a ratio of 9 : 1. The CRC-VAL-HE-7K is treated as the test set.

89 *ChestMNIST*

90 The ChestMNIST is based on the NIH-ChestXray14 dataset¹⁸, a dataset comprising 112,120 frontal-view X-Ray images
 91 of 30,805 unique patients with the text-mined 14 disease labels, which could be formulized as a multi-label binary-class
 92 classification task. We use the official data split, and resize the source images of $1 \times 1,024 \times 1,024$ into $1 \times 28 \times 28$.

93 *DermaMNIST*

94 The DermaMNIST is based on the HAM10000¹⁹⁻²¹, a large collection of multi-source dermatoscopic images of common
 95 pigmented skin lesions. The dataset consists of 10,015 dermatoscopic images categorized as 7 different diseases, formulized as
 96 a multi-class classification task. We split the images into training, validation and test set with a ratio of 7 : 1 : 2. The source
 97 images of $3 \times 600 \times 450$ are resized into $3 \times 28 \times 28$.

98 *OCTMNIST*

99 The OCTMNIST is based on a prior dataset^{22,23} of 109,309 valid optical coherence tomography (OCT) images for retinal
 100 diseases. The dataset is comprised of 4 diagnosis categories, leading to a multi-class classification task. We split the source
 101 training set with a ratio of 9 : 1 into training and validation set, and use its source validation set as the test set. The source
 102 images are gray-scale, and their sizes are $(384 - 1,536) \times (277 - 512)$. We center-crop the images with a window size of
 103 length of the short edge and resize them into $1 \times 28 \times 28$.

104 **PneumoniaMNIST**

105 The PneumoniaMNIST is based on a prior dataset^{22,23} of 5,856 pediatric chest X-Ray images. The task is binary-class
106 classification of pneumonia against normal. We split the source training set with a ratio of 9 : 1 into training and validation set,
107 and use its source validation set as the test set. The source images are gray-scale, and their sizes are $(384 - 2,916) \times (127 -$
108 $2,713)$. We center-crop the images with a window size of length of the short edge and resize them into $1 \times 28 \times 28$.

109 **RetinaMNIST**

110 The RetinaMNIST is based on the DeepDRiD²⁴ challenge, which provides a dataset of 1,600 retina fundus images. The task
111 is ordinal regression for 5-level grading of diabetic retinopathy severity. We split the source training set with a ratio of 9 : 1
112 into training and validation set, and use the source validation set as the test set. The source images of $3 \times 1,736 \times 1,824$ are
113 center-cropped with a window size of length of the short edge and resized into $3 \times 28 \times 28$.

114 **BreastMNIST**

115 The BreastMNIST is based on a dataset²⁵ of 780 breast ultrasound images. It is categorized into 3 classes: normal, benign, and
116 malignant. As we use low-resolution images, we simplify the task into binary classification by combining normal and benign as
117 positive and classifying them against malignant as negative. We split the source dataset with a ratio of 7 : 1 : 2 into training,
118 validation and test set. The source images of $1 \times 500 \times 500$ are resized into $1 \times 28 \times 28$.

119 **BloodMNIST**

120 The BloodMNIST is based on a dataset^{26,27} of individual normal cells, captured from individuals without infection, hematologic
121 or oncologic disease and free of any pharmacologic treatment at the moment of blood collection. It contains a total of 17,092
122 images and is organized into 8 classes. We split the source dataset with a ratio of 7 : 1 : 2 into training, validation and test
123 set. The source images with resolution $3 \times 360 \times 363$ pixels are center-cropped into $3 \times 200 \times 200$, and then resized into
124 $3 \times 28 \times 28$.

125 **TissueMNIST**

126 We use the BBBC051³⁴, available from the Broad Bioimage Benchmark Collection²⁸. The dataset contains 236,386 human
127 kidney cortex cells, segmented from 3 reference tissue specimens and organized into 8 categories. We split the source dataset
128 with a ratio of 7 : 1 : 2 into training, validation and test set. Each gray-scale image is $32 \times 32 \times 7$ pixels, where 7 denotes 7
129 slices. We obtain 2D maximum projections by taking the maximum pixel value along the axial-axis of each pixel, and resize
130 them into 28×28 gray-scale images.

131 **Organ{A,C,S}MNIST**

132 The Organ{A,C,S}MNIST is based on 3D computed tomography (CT) images from Liver Tumor Segmentation Benchmark
133 (LiTS)²⁹. They are renamed from OrganMNIST_{Axial,Coronal,Sagittal} (in MedMNIST v1⁹) for simplicity. We use bounding-
134 box annotations of 11 body organs from another study³⁰ to obtain the organ labels. Hounsfield-Unit (HU) of the 3D images are
135 transformed into gray-scale with an abdominal window. We crop 2D images from the center slices of the 3D bounding boxes in
136 axial / coronal / sagittal views (planes). The only differences of Organ{A,C,S}MNIST are the views. The images are resized
137 into $1 \times 28 \times 28$ to perform multi-class classification of 11 body organs. 115 and 16 CT scans from the source training set are
138 used as training and validation set, respectively. The 70 CT scans from the source test set are treated as the test set.

139 **Details for MedMNIST3D**

140 **OrganMNIST3D**

141 The source of the OrganMNIST3D is the same as that of the Organ{A,C,S}MNIST. Instead of 2D images, we directly use
142 the 3D bounding boxes and process the images into $28 \times 28 \times 28$ to perform multi-class classification of 11 body organs. The
143 same 115 and 16 CT scans as the Organ{A,C,S}MNIST from the source training set are used as training and validation set,
144 respectively, and the same 70 CT scans as the Organ{A,C,S}MNIST from the source test set are treated as the test set.

145 **NoduleMNIST3D**

146 The NoduleMNIST3D is based on the LIDC-IDRI³¹, a large public lung nodule dataset, containing images from thoracic CT
147 scans. The dataset is designed for both lung nodule segmentation and 5-level malignancy classification task. To perform binary
148 classification, we categorize cases with malignancy level 1/2 into negative class and 4/5 into positive class, ignoring the cases
149 with malignancy level 3. We split the source dataset with a ratio of 7 : 1 : 2 into training, validation and test set, and center-crop
150 the spatially normalized images (with a spacing of $1mm \times 1mm \times 1mm$) into $28 \times 28 \times 28$.

151 **AdrenalMNIST3D**

152 The AdrenalMNIST3D is a new 3D shape classification dataset, consisting of shape masks from 1,584 left and right adrenal
153 glands (*i.e.*, 792 patients). Collected from Zhongshan Hospital Affiliated to Fudan University, each 3D shape of adrenal gland
154 is annotated by an expert endocrinologist using abdominal computed tomography (CT), together with a binary classification
155 label of normal adrenal gland or adrenal mass. Considering patient privacy, we do not provide the source CT scans, but the real
156 3D shapes of adrenal glands and their classification labels. We calculate the center of adrenal and resize the center-cropped
157 $64mm \times 64mm \times 64mm$ volume into $28 \times 28 \times 28$. The dataset is randomly split into training / validation / test set of 1,188 / 98
158 / 298 on a patient level.

159 **FractureMNIST3D**

160 The FractureMNIST3D is based on the RibFrac Dataset³², containing around 5,000 rib fractures from 660 computed tomography
161 (CT) scans. The dataset organizes detected rib fractures into 4 clinical categories (*i.e.*, buckle, nondisplaced, displaced, and
162 segmental rib fractures). As we use low-resolution images, we disregard segmental rib fractures and classify 3 types of rib
163 fractures (*i.e.*, buckle, nondisplaced, and displaced). For each annotated fracture area, we calculate its center and resize the
164 center-cropped $64mm \times 64mm \times 64mm$ image into $28 \times 28 \times 28$. The official split of training, validation and test set is used.

165 **VesselMNIST3D**

166 The VesselMNIST3D is based on an open-access 3D intracranial aneurysm dataset, Intra³³, containing 103 3D models (meshes)
167 of entire brain vessels collected by reconstructing MRA images. 1,694 healthy vessel segments and 215 aneurysm segments
168 are generated automatically from the complete models. We fix the non-watertight mesh with PyMeshFix³⁵ and voxelize the
169 watertight mesh with trimesh³⁶ into $28 \times 28 \times 28$ voxels. We split the source dataset with a ratio of 7 : 1 : 2 into training,
170 validation and test set.

171 **SynapseMNIST3D**

172 The SynapseMNIST3D is a new 3D volume dataset to classify whether a synapse is excitatory or inhibitory. It uses a 3D
173 image volume of an adult rat acquired by a multi-beam scanning electron microscope. The original data is of the size
174 $100 \times 100 \times 100um^3$ and the resolution $8 \times 8 \times 30nm^3$, where a $(30um)^3$ sub-volume was used in the MitoEM dataset³⁷ with
175 dense 3D mitochondria instance segmentation labels. Three neuroscience experts segment a pyramidal neuron within the whole
176 volume and proofread all the synapses on this neuron with excitatory / inhibitory labels. For each labeled synaptic location, we
177 crop a 3D volume of $1024 \times 1024 \times 1024nm^3$ and resize it into $28 \times 28 \times 28$ voxels. Finally, the dataset is randomly split with
178 a ratio of 7 : 1 : 2 into training, validation and test set.

179 **Data Records**

180 The data files of MedMNIST v2 dataset can be accessed at Zenodo³⁸. It contains 12 pre-processed 2D datasets (MedMNIST2D)
181 and 6 pre-processed 3D datasets (MedMNIST3D). Each subset is saved in NumPy³⁹ npz format, named as <data>mnist.npz
182 for MedMNIST2D and <data>mnist3d.npz for MedMNIST3D, and is comprised of 6 keys (“train_images”, “train_labels”,
183 “val_images”, “val_labels”, “test_images”, “test_labels”). The data type of the dataset is uint8.

- 184 • “{train,val,test}_images”: an array containing images, with a shape of $N \times 28 \times 28$ for 2D gray-scale datasets, of
185 $N \times 28 \times 28 \times 3$ for 2D RGB datasets, of $N \times 28 \times 28 \times 28$ for 3D datasets. N denotes the number of samples in training
186 / validation / test set.
- 187 • “{train,val,test}_labels”: an array containing ground-truth labels, with a shape of $N \times 1$ for multi-class / binary-class /
188 ordinal regression datasets, of $N \times L$ for multi-lable binary-class datasets. N denotes the number of samples in training /
189 validation / test set and L denotes the number of task labels in the multi-label dataset (*i.e.*, 14 for the ChestMNIST).

190 **Technical Validation**

191 **Baseline Methods**

192 For MedMNIST2D, we first implement ResNets¹⁰ with a simple early-stopping strategy on validation set as baseline methods.
193 The ResNet model contains 4 residual layers and each layer has several blocks, which is a stack of convolutional layers, batch
194 normalization and ReLU activation. The input channel is always 3 since we convert gray-scale images into RGB images. To
195 fairly compare with other methods, the input resolutions are 28 or 224 (resized from 28) for the ResNet-18 and ResNet-50.
196 For all model training, we use cross entropy-loss and set the batch size as 128. We utilize an Adam optimizer⁴⁰ with an initial
197 learning rate of 0.001 and train the model for 100 epochs, delaying the learning rate by 0.1 after 50 and 75 epochs.

198 For MedMNIST3D, we implement ResNet-18 / ResNet-50¹⁰ with 2.5D / 3D / ACS⁴¹ convolutions with a simple early-
199 stopping strategy on validation set as baseline methods, using the one-line 2D neural network converters provided in the official

ACS code repository (<https://github.com/M3DV/ACSCov>). When loading the datasets, we copy the single channel into 3 channels to make it compatible. For all model training, we use cross-entropy loss and set the batch size as 32. We utilize an Adam optimizer⁴⁰ with an initial learning rate of 0.001 and train the model for 100 epochs, delaying the learning rate by 0.1 after 50 and 75 epochs. Additionally, as a regularization for the two datasets of shape modality (*i.e.*, AdrenalMNIST3D / VesselMNIST3D), we multiply the training set by a random value in [0, 1] during training and multiply the images by a fixed coefficient of 0.5 during evaluation.

The details of model implementation and training scheme can be found in our code.

AutoML Methods

We have also selected several AutoML methods: auto-sklearn¹¹ as the representative of open-source AutoML tools for statistical machine learning, AutoKeras¹² as the representative of open-source AutoML tools for deep learning, and Google AutoML Vision as the representative of commercial black-box AutoML tools, with deep learning empowered. We run auto-sklearn¹¹ and AutoKeras¹² on both MedMNIST2D and MedMNIST3D, and Google AutoML Vision on MedMNIST2D only.

auto-sklearn¹¹ automatically searches the algorithms and hyper-parameters in scikit-learn⁴² package. We set time limit for search of appropriate models according to the dataset scale. The time limit is 2 hours for 2D datasets with scale < 10,000, 4 hours for those of [10,000,50,000], and 6 hours for those > 50,000. For 3D datasets, we set time limit as 4 hours. We flatten the images into one dimension, and provide reshaped one-dimensional data with the corresponding labels for auto-sklearn to fit.

AutoKeras¹² based on Keras package⁴³ searches deep neural networks and hyper-parameters. For each dataset, we set number of max_trials as 20 and number of epochs as 20. It tries 20 different Keras models and trains each model for 20 epochs. We choose the best model based on the highest AUC score on validation set.

Google AutoML Vision (<https://cloud.google.com/vision/automl/docs>, experimented in July, 2021) is a commercial AutoML tool offered as a service from Google Cloud. We train Edge exportable models of MedMNIST2D on Google AutoML Vision and export trained quantized models into TensorFlow Lite format to do offline inference. We set number of node hours of each dataset according to the data scale. We allocate 1 node hour for dataset with scale around 1,000, 2 node hours for scale around 10,000, 3 node hours for scale around 100,000, and 4 node hours for scale around 200,000.

Evaluation

Area under ROC curve (AUC)⁴⁴ and Accuracy (ACC) are used as the evaluation metrics. AUC is a threshold-free metric to evaluate the continuous prediction scores, while ACC evaluates the discrete prediction labels given threshold (or argmax). AUC is less sensitive to class imbalance than ACC. Since there is no severe class imbalance on our datasets, ACC could also serve as a good metric. Although there are many other metrics, we simply select AUC and ACC for the sake of simplicity and standardization of evaluation. We report the AUC and ACC for each dataset. Data users are also encouraged to analyze the average performance over the 12 2D datasets and 6 3D datasets to benchmark their methods. Thereby, we report average AUC and ACC score over MedMNIST2D and MedMNIST3D respectively to easily compare the performance of different methods.

Benchmark on Each Dataset

The performance on each dataset of MedMNIST2D and MedMNIST3D is reported in Table 3 and Table 4, respectively. We calculate the mean value of at least 3 trials for each method on each dataset.

For 2D datasets, Google AutoML Vision is well-performing in general, however it could not always win, even compared with the baseline ResNet-18 and ResNet-50. Auto-sklearn performs poorly on most datasets, indicating that the typical statistical machine learning algorithms do not work well on our 2D medical image datasets. AutoKeras performs well on datasets with large scales, however relatively worse on datasets with small scale. With the same depth of ResNet backbone, datasets of resolution 224 outperform resolution 28 in general. For datasets of resolution 28, ResNet-18 wins higher scores than ResNet-50 on most datasets.

For 3D datasets, AutoKeras does not work well, while auto-sklearn performs better than on MedMNIST2D. Auto-sklearn is superior to ResNet-18+2.5D and ResNet-50+2.5D in general, and even outperforms all the other methods in ACC score on AdrenalMNIST3D. 2.5D models have poorer performance compared with 3D and ACS models, while 3D and ACS models are comparable to each other. With 3D convolution, ResNet-50 backbone surpasses ResNet-18.

Average Performance of Each Method

To compare the performance of various methods, we report the average AUC and average ACC of each method over all datasets. The average performance of methods on MedMNIST2D and MedMNIST3D are reported in Table 5 and Table 6, respectively. Despite the great gap among the metrics of different sub-datasets, the average AUC and ACC could still manifest the performance of each method.

For MedMNIST2D, Google AutoML Vision outperforms all the other methods in average AUC, however, it is very close to the performance of baseline ResNets. The ResNets surpass auto-sklearn and AutoKeras, and outperform Google AutoML

Table 3. Benchmark on each dataset of MedMNIST2D in metrics of AUC and ACC.

Methods	PathMNIST		ChestMNIST		DermaMNIST		OCTMNIST		PneumoniaMNIST		RetinaMNIST	
	AUC	ACC	AUC	ACC	AUC	ACC	AUC	ACC	AUC	ACC	AUC	ACC
ResNet-18 (28) ¹⁰	0.983	0.907	0.768	0.947	0.917	0.735	0.943	0.743	0.944	0.854	0.717	0.524
ResNet-18 (224) ¹⁰	0.989	0.909	0.773	0.947	0.920	0.754	0.958	0.763	0.956	0.864	0.710	0.493
ResNet-50 (28) ¹⁰	0.990	0.911	0.769	0.947	0.913	0.735	0.952	0.762	0.948	0.854	0.726	0.528
ResNet-50 (224) ¹⁰	0.989	0.892	0.773	0.948	0.912	0.731	0.958	0.776	0.962	0.884	0.716	0.511
auto-sklearn ¹¹	0.934	0.716	0.649	0.779	0.902	0.719	0.887	0.601	0.942	0.855	0.690	0.515
AutoKeras ¹²	0.959	0.834	0.742	0.937	0.915	0.749	0.955	0.763	0.947	0.878	0.719	0.503
Google AutoML Vision	0.944	0.728	0.778	0.948	0.914	0.768	0.963	0.771	0.991	0.946	0.750	0.531

Methods	BreastMNIST		BloodMNIST		TissueMNIST		OrganAMNIST		OrganCMNIST		OrganSMNIST	
	AUC	ACC	AUC	ACC	AUC	ACC	AUC	ACC	AUC	ACC	AUC	ACC
ResNet-18 (28) ¹⁰	0.901	0.863	0.998	0.958	0.930	0.676	0.997	0.935	0.992	0.900	0.972	0.782
ResNet-18 (224) ¹⁰	0.891	0.833	0.998	0.963	0.933	0.681	0.998	0.951	0.994	0.920	0.974	0.778
ResNet-50 (28) ¹⁰	0.857	0.812	0.997	0.956	0.931	0.680	0.997	0.935	0.992	0.905	0.972	0.770
ResNet-50 (224) ¹⁰	0.866	0.842	0.997	0.950	0.932	0.680	0.998	0.947	0.993	0.911	0.975	0.785
auto-sklearn ¹¹	0.836	0.803	0.984	0.878	0.828	0.532	0.963	0.762	0.976	0.829	0.945	0.672
AutoKeras ¹²	0.871	0.831	0.998	0.961	0.941	0.703	0.994	0.905	0.990	0.879	0.974	0.813
Google AutoML Vision	0.919	0.861	0.998	0.966	0.924	0.673	0.990	0.886	0.988	0.877	0.964	0.749

Table 4. Benchmark on each dataset of MedMNIST3D in metrics of AUC and ACC.

Methods	OrganMNIST3D		NoduleMNIST3D		FractureMNIST3D		AdrenalMNIST3D		VesselMNIST3D		SynapseMNIST3D	
	AUC	ACC	AUC	ACC	AUC	ACC	AUC	ACC	AUC	ACC	AUC	ACC
ResNet-18 ¹⁰ +2.5D	0.977	0.788	0.838	0.835	0.587	0.451	0.718	0.772	0.748	0.846	0.634	0.696
ResNet-18 ¹⁰ +3D	0.996	0.907	0.863	0.844	0.712	0.508	0.827	0.721	0.874	0.877	0.820	0.745
ResNet-18 ¹⁰ +ACS ⁴¹	0.994	0.900	0.873	0.847	0.714	0.497	0.839	0.754	0.930	0.928	0.705	0.722
ResNet-50 ¹⁰ +2.5D	0.974	0.769	0.835	0.848	0.552	0.397	0.732	0.763	0.751	0.877	0.669	0.735
ResNet-50 ¹⁰ +3D	0.994	0.883	0.875	0.847	0.725	0.494	0.828	0.745	0.907	0.918	0.851	0.795
ResNet-50 ¹⁰ +ACS ⁴¹	0.994	0.889	0.886	0.841	0.750	0.517	0.828	0.758	0.912	0.858	0.719	0.709
auto-sklearn ¹¹	0.977	0.814	0.914	0.874	0.628	0.453	0.828	0.802	0.910	0.915	0.631	0.730
AutoKeras ¹²	0.979	0.804	0.844	0.834	0.642	0.458	0.804	0.705	0.773	0.894	0.538	0.724

252 Vision in average ACC. Under the same backbone, the datasets with resolution of 224 win higher AUC and ACC score than
 253 resolution of 28. While under the same resolution, ResNet-18 is superior to ResNet-50.

254 For MedMNIST3D, AutoKeras does not perform well, performing worse than auto-sklearn. Under the same ResNet
 255 backbone, 2.5D models are inferior to 3D and ACS models and perform worse than auto-sklearn and AutoKeras. Surprisingly,
 256 the ResNet-50 with standard 3D convolution outperforms all the other methods on average.

Table 5. Average performance of MedMNIST2D in metrics of average AUC and average ACC over all 2D datasets.

Methods	AVG AUC	AVG ACC
ResNet-18 (28) ¹⁰	0.922	0.819
ResNet-18 (224) ¹⁰	0.925	0.821
ResNet-50 (28) ¹⁰	0.920	0.816
ResNet-50 (224) ¹⁰	0.923	0.821
auto-sklearn ¹¹	0.878	0.722
AutoKeras ¹²	0.917	0.813
Google AutoML Vision	0.927	0.809

257 **Difference between Organ{A,C,S}MNIST and OrganMNIST3D**

258 Organ{A,C,S}MNIST and OrganMNIST3D are generated from the same source dataset, and share the same task and the same
 259 data split. However, samples in the 2D and 3D datasets are different. Organ{A,C,S}MNIST are sampled slices of 3D bounding

Table 6. Average performance of MedMNIST3D in metrics of average AUC and average ACC over all 3D datasets.

Methods	AVG AUC	AVG ACC
ResNet-18 ¹⁰ +2.5D	0.750	0.731
ResNet-18 ¹⁰ +3D	0.849	0.767
ResNet-18 ¹⁰ +ACS ⁴¹	0.842	0.775
ResNet-50 ¹⁰ +2.5D	0.752	0.732
ResNet-50 ¹⁰ +3D	0.863	0.780
ResNet-50 ¹⁰ +ACS ⁴¹	0.848	0.762
auto-sklearn ¹¹	0.815	0.765
AutoKeras ¹²	0.763	0.737

260 boxes of 3D CT images in axial / coronal / sagittal views (planes), respectively. They are sliced before being resized into
 261 $1 \times 28 \times 28$. On the other hand, OrganMNIST3D is resized into $28 \times 28 \times 28$ directly. Therefore, the Organ{A,C,S}MNIST
 262 metrics in Table 3 and the OrganMNIST3D metrics in Table 4 should not be compared.

263 We perform experiments to clarify the difference between Organ{A,C,S}MNIST and OrganMNIST3D. We slice the
 264 OrganMNIST3D dataset in the axial / coronal / sagittal views (planes) respectively to generate the central slices. For each
 265 view, we take the 60% central slices when slicing and discard the other 40% slices. We evaluate the model performance on the
 266 OrganMNIST3D, with 2D-input ResNet-18 trained with Organ{A,C,S}MNIST and the axial / coronal / sagittal central slices of
 267 OrganMNIST3D, as well as 3D-input ResNet-18. The results are reported in Table 7. The performance of 3D-input models is
 268 comparable to that of 2D-input models with axial view in general. In other words, with an appropriate setting, the 2D inputs
 269 and 3D inputs are comparable on the OrganMNIST3D dataset.

Table 7. Model performance on OrganMNIST3D test set in various settings, including (upper) 2D-input ResNet-18¹⁰ trained with Organ{A,C,S}MNIST and axial / coronal / sagittal central slices of OrganMNIST3D, and (lower) 3D-input ResNet-18 with 2.5D / 3D / ACS⁴¹ convolutions, trained with OrganMNIST3D (same as Table 4).

Methods	AUC	ACC
<i>2D-Input ResNet-18</i>		
Trained with OrganAMNIST	0.995	0.907
Trained with axial central slices of OrganMNIST3D	0.995	0.916
Trained with OrganCMNIST	0.991	0.877
Trained with coronal central slices of OrganMNIST3D	0.992	0.890
Trained with OrganSMNIST	0.959	0.697
Trained with sagittal central slices of OrganMNIST3D	0.963	0.701
<i>3D-Input ResNet-18</i>		
2.5D trained with OrganMNIST3D	0.977	0.788
3D trained with OrganMNIST3D	0.996	0.907
ACS trained with OrganMNIST3D	0.994	0.900

270 Usage Notes

271 The MedMNIST can be freely available at <https://medmnist.com/>. We would be grateful if the users of MedMNIST
 272 dataset could cite MedMNIST v1⁹ and v2 (this paper), as well as the corresponding source dataset in the publications.

273 Please note that this dataset is NOT intended for clinical use, as substantially reducing the resolution of medical images
 274 might result in images that are insufficient to represent and capture different disease pathologies.

275 Code availability

276 The data API and evaluation script in Python is available at <https://github.com/MedMNIST/MedMNIST>. The
 277 reproducible experiment codebase is available at <https://github.com/MedMNIST/experiments>.

278 Acknowledgements

279 This work was supported by National Science Foundation of China (U20B200011, 61976137). This work was also supported by
280 Grant YG2021ZD18 from Shanghai Jiao Tong University Medical Engineering Cross Research. We would like to acknowledge
281 all authors of the open datasets used in this study.

282 Author contributions statement

283 JY conceived the experiments. JY and RS developed the code and benchmark. JY, RS, DW, ZL, LZ, BK and HP contributed to
284 data collection, cleaning and annotations. JY, RS, DW and BN wrote the manuscript. All authors reviewed the manuscript.

285 Competing interests

286 The authors declare no competing interests.

287 References

- 288 1. Shen, D., Wu, G. & Suk, H.-I. Deep learning in medical image analysis. *Annu. review biomedical engineering* **19**, 221–248
289 (2017).
- 290 2. Litjens, G. *et al.* A survey on deep learning in medical image analysis. *Med. image analysis* **42**, 60–88 (2017).
- 291 3. Liu, X. *et al.* A comparison of deep learning performance against health-care professionals in detecting diseases from
292 medical imaging: a systematic review and meta-analysis. *The lancet digital health* **1**, e271–e297 (2019).
- 293 4. Rebuffi, S.-A., Bilen, H. & Vedaldi, A. Learning multiple visual domains with residual adapters. In *Advances in Neural*
294 *Information Processing Systems*, 506–516 (2017).
- 295 5. Simpson, A. L. *et al.* A large annotated medical image dataset for the development and evaluation of segmentation
296 algorithms. Preprint at <https://arxiv.org/abs/1902.09063> (2019).
- 297 6. Antonelli, M. *et al.* The medical segmentation decathlon. Preprint at <https://arxiv.org/abs/2106.05735> (2021).
- 298 7. Isensee, F., Jaeger, P. F., Kohl, S. A., Petersen, J. & Maier-Hein, K. H. nnu-net: a self-configuring method for deep
299 learning-based biomedical image segmentation. *Nat. methods* **18**, 203–211 (2021).
- 300 8. LeCun, Y., Cortes, C. & Burges, C. Mnist handwritten digit database. <http://yann.lecun.com/exdb/mnist/> (2010).
- 301 9. Yang, J., Shi, R. & Ni, B. Medmnist classification decathlon: A lightweight automl benchmark for medical image analysis.
302 In *International Symposium on Biomedical Imaging*, 191–195 (2021).
- 303 10. He, K., Zhang, X., Ren, S. & Sun, J. Deep residual learning for image recognition. In *Conference on Computer Vision and*
304 *Pattern Recognition*, 770–778 (2016).
- 305 11. Feurer, M. *et al.* Auto-sklearn: efficient and robust automated machine learning. In *Automated Machine Learning*, 113–134
306 (Springer, Cham, 2019).
- 307 12. Jin, H., Song, Q. & Hu, X. Auto-keras: An efficient neural architecture search system. In *Conference on Knowledge*
308 *Discovery and Data Mining*, 1946–1956 (ACM, 2019).
- 309 13. Qi, K. & Yang, H. Elastic net nonparallel hyperplane support vector machine and its geometrical rationality. *IEEE*
310 *Transactions on Neural Networks Learn. Syst.* (2021).
- 311 14. Chen, K. *et al.* Alleviating data imbalance issue with perturbed input during inference. In *Conference on Medical Image*
312 *Computing and Computer Assisted Intervention*, 407–417 (Springer, 2021).
- 313 15. Henn, T. *et al.* A principled approach to failure analysis and model repairment: Demonstration in medical imaging. In
314 *Conference on Medical Image Computing and Computer Assisted Intervention*, 509–518 (Springer, 2021).
- 315 16. Kather, J. N. *et al.* Predicting survival from colorectal cancer histology slides using deep learning: A retrospective
316 multicenter study. *PLOS Medicine* **16**, 1–22, <https://doi.org/10.1371/journal.pmed.1002730> (2019).
- 317 17. Kather, J. N., Halama, N. & Marx, A. 100,000 histological images of human colorectal cancer and healthy tissue,
318 <https://doi.org/10.5281/zenodo.1214456> (2018).
- 319 18. Wang, X. *et al.* Chestx-ray8: Hospital-scale chest x-ray database and benchmarks on weakly-supervised classification and
320 localization of common thorax diseases. In *Conference on Computer Vision and Pattern Recognition*, 3462–3471 (2017).
- 321 19. Tschandl, P., Rosendahl, C. & Kittler, H. The ham10000 dataset, a large collection of multi-source dermatoscopic images
322 of common pigmented skin lesions. *Sci. data* **5**, 180161 (2018).

- 323 **20.** Tschandl, P. The HAM10000 dataset, a large collection of multi-source dermatoscopic images of common pigmented skin
324 lesions, <https://doi.org/10.7910/DVN/DBW86T> (2018).
- 325 **21.** Codella, N. *et al.* Skin lesion analysis toward melanoma detection 2018: A challenge hosted by the international skin
326 imaging collaboration (isic). Preprint at <https://arxiv.org/abs/1902.03368v2> (2019).
- 327 **22.** Kermany, D. S. *et al.* Identifying medical diagnoses and treatable diseases by image-based deep learning. *Cell* **172**, 1122 –
328 1131.e9, <https://doi.org/10.1016/j.cell.2018.02.010> (2018).
- 329 **23.** Kermany, D. S., Zhang, K. & Goldbaum, M. Large dataset of labeled optical coherence tomography (oct) and chest x-ray
330 images, <https://doi.org/10.17632/rscbjbr9sj.3> (2018).
- 331 **24.** DeepDRiD. The 2nd diabetic retinopathy – grading and image quality estimation challenge. <https://isbi.deepdr.org/data.html>
332 (2020).
- 333 **25.** Al-Dhabyani, W., Gomaa, M., Khaled, H. & Fahmy, A. Dataset of breast ultrasound images. *Data Brief* **28**, 104863,
334 <https://doi.org/10.1016/j.dib.2019.104863> (2020).
- 335 **26.** Acevedo, A. *et al.* A dataset of microscopic peripheral blood cell images for development of automatic recognition systems.
336 *Data Brief* **30**, 105474, <https://doi.org/10.1016/j.dib.2020.105474> (2020).
- 337 **27.** Acevedo, A. *et al.* A dataset for microscopic peripheral blood cell images for development of automatic recognition
338 systems, <https://doi.org/10.17632/snkd93bnjr.1> (2020).
- 339 **28.** Ljosa, V., Sokolnicki, K. L. & Carpenter, A. E. Annotated high-throughput microscopy image sets for validation. *Nat.*
340 *methods* **9**, 637–637 (2012).
- 341 **29.** Bilic, P. *et al.* The liver tumor segmentation benchmark (lits). Preprint at <https://arxiv.org/abs/1901.04056> (2019).
- 342 **30.** Xu, X., Zhou, F. *et al.* Efficient multiple organ localization in ct image using 3d region proposal network. *IEEE Transactions*
343 *on Med. Imaging* **38**, 1885–1898 (2019).
- 344 **31.** Armato III, S. G. *et al.* The lung image database consortium (lidc) and image database resource initiative (idri): A
345 completed reference database of lung nodules on ct scans. *Med. Phys.* **38**, 915–931, <https://doi.org/10.1118/1.3528204>
346 (2011). <https://aapm.onlinelibrary.wiley.com/doi/pdf/10.1118/1.3528204>.
- 347 **32.** Jin, L. *et al.* Deep-learning-assisted detection and segmentation of rib fractures from ct scans: Development and validation
348 of fracnet. *EBioMedicine* **62**, 103106, <https://doi.org/10.1016/j.ebiom.2020.103106> (2020).
- 349 **33.** Yang, X., Xia, D., Kin, T. & Igarashi, T. Intra: 3d intracranial aneurysm dataset for deep learning. In *Conference on*
350 *Computer Vision and Pattern Recognition* (2020).
- 351 **34.** Woloshuk, A. *et al.* In situ classification of cell types in human kidney tissue using 3d nuclear staining. *Cytom. Part A*
352 (2020).
- 353 **35.** Attene, M. A lightweight approach to repairing digitized polygon meshes. *The Vis. Comput.* **26**, 1393–1406 (2010).
- 354 **36.** Dawson-Haggerty *et al.* trimesh. <https://trimsh.org/> (2019).
- 355 **37.** Wei, D. *et al.* Mitoem dataset: Large-scale 3d mitochondria instance segmentation from em images. In *Conference on*
356 *Medical Image Computing and Computer Assisted Intervention*, 66–76 (Springer, 2020).
- 357 **38.** Yang, J. *et al.* Medmnist v2: A large-scale lightweight benchmark for 2d and 3d biomedical image classification,
358 <https://doi.org/10.5281/zenodo.5208230> (2021).
- 359 **39.** Harris, C. R. *et al.* Array programming with numpy. *Nature* **585**, 357–362 (2020).
- 360 **40.** Kingma, D. P. & Ba, J. Adam: A method for stochastic optimization. Preprint at <https://arxiv.org/abs/1412.6980> (2014).
- 361 **41.** Yang, J. *et al.* Reinventing 2d convolutions for 3d images. *IEEE J. Biomed. Heal. Informatics* 1–1, <https://doi.org/10.1109/JBHI.2021.3049452> (2021).
- 362 **42.** Pedregosa, F. *et al.* Scikit-learn: Machine learning in python. *J. machine Learn. research* **12**, 2825–2830 (2011).
- 363 **43.** Chollet, F. *et al.* Keras. <https://keras.io> (2015).
- 364 **44.** Bradley, A. P. The use of the area under the roc curve in the evaluation of machine learning algorithms. *Pattern recognition*
365 **30**, 1145–1159 (1997).
- 366